Stability of Free Surface Ekman Layers

GEORGE F. SPOONER[1]

Ocean Dynamics Branch, Naval Research Laboratory, Washington, DC 20375

(Manuscript received 8 September 1982, in final form 13 December 1982)

ABSTRACT

The stability of free surface, laminar Ekman layers is examined for both the homogeneous and the two-layer case. The eigenvalues of the homogeneous case depend upon the wavenumbers α and γ and the Reynolds number Re. Those of the two-layer case depend upon α, γ, Re, the depth of the top layer, and the parameter $\mathrm{Fr}^* = g\delta(\rho^* - \rho)/(U_s^2\rho)$, where g is the acceleration of gravity, δ is the Ekman scaling depth, ρ and ρ^* are the densities of the top and bottom layers, respectively, and U_s is the mean speed at the surface. The behavior of the inflection point mode and the parallel mode of instability is examined as a function of the independent parameters in both cases.

1. Introduction

The hydrodynamic stability of the laminar Ekman boundary layer is a subject which has attracted a great deal of attention. It has been the subject of a number of studies over a period of some twenty years. Experimental investigations have included those of Faller (1963), and Tatro and Mollo-Christensen (1967). The problem has been treated theoretically by Faller and Kaylor (1966, 1967), Lilly (1966), Brown (1970), and Iooss *et al.* (1978).

With the exception of a short treatment by Faller and Kaylor (1967) and brief mention by Iooss *et al.* (1978), the free surface Ekman stability problem has been neglected in favor of the problem which possesses a rigid lower boundary. As Faller and Kaylor (1967) point out, however, there is a fundamental difference between the two cases. The disturbances in the rigid boundary problem are constrained to vanish at the boundary, whereas this is not so for the free surface problem.

Since the free surface case is much more akin to what might occur in the oceanic boundary layer, it is worthwhile to examine the problem a bit more closely, with an eye toward determining the structure and distribution of the various modes of instability which may exist. Such knowledge is necessary, for example, if one is desirous of solving the initial value problem for this case, as has been done for a rigidly bounded Ekman layer by Spooner and Criminale (1982).

Two different examples of a free surface Ekman layer will be considered. The first will be an Ekman layer in a homogeneous fluid. This is the problem which was examined by Faller and Kaylor (1967) and Iooss *et al.* (1978).

The second example will be an Ekman layer in a two layer fluid. Such a situation might arise, for instance, when an Ekman layer is established in a pre-existing mixed layer. Although the stability of a continuously stratified Ekman layer has been considered by Faller and Kaylor (1967), Etling (1971), Kaylor and Faller (1972) and Brown (1972), the author is not aware of any work which has been done on the two layer case. It will be seen that, in both these examples, the eigenvalue distribution and eigenfunction structure depart markedly from the rigid boundary case.

2. The homogeneous case

a. Derivation of the perturbation equations

The physical system which is to be considered is a rotating, homogeneous, incompressible fluid. The system is governed by the equations of motion and the incompressibility condition.

$$\left.\begin{aligned} \frac{d\bar{u}}{dt} - f\bar{v} &= -\frac{1}{\rho}\frac{\partial \bar{p}}{\partial x} + \nu\nabla^2\bar{u} \\ \frac{d\bar{v}}{dt} + f\bar{u} &= -\frac{1}{\rho}\frac{\partial \bar{p}}{\partial y} + \nu\nabla^2\bar{v} \\ \frac{d\bar{w}}{dt} &= -\frac{1}{\rho}\frac{\partial \bar{p}}{\partial z} + \nu\nabla^2\bar{w} \\ \frac{\partial \bar{u}}{\partial x} + \frac{\partial \bar{v}}{\partial y} + \frac{\partial \bar{w}}{\partial z} &= 0 \end{aligned}\right\}. \tag{1}$$

The coordinate system is right-handed, with z directed positive upward. The velocity components in the x, y and z directions are $\bar{u}$, $\bar{v}$ and $\bar{w}$, respectively. The remaining quantities are the pressure $\bar{p}$, density

[1] Current address: 111 W. Smith St., Seattle, WA 98119.

ρ, the Coriolis parameter f, and kinematic viscosity ν. The Laplacian operator is represented by ∇^2.

The unknown quantities are now regarded as the sum of a mean and a fluctuating part.

$$\bar{u} = U + u,$$
$$\text{etc.}$$

The mean quantities, represented by upper case letters, are time independent. The fluctuating portions are represented by lower case letters. Substitution of these sums into (1) and taking a time average yields equations for the time independent mean flow. In the present case, that of an oceanic Ekman layer, the solutions of these equations will be

$$U = U_s \exp(z/\delta)\cos(z/\delta),$$
$$V = U_s \exp(z/\delta)\sin(z/\delta),$$

where U_s is the magnitude of the velocity at the surface, and $\delta = (2\nu/f)^{1/2}$.

The perturbation equations are formed by subtracting the mean flow equations from those which result when the quantities in (1) are assumed to be the sum of a mean and a fluctuating part. Assuming that the amplitudes of the perturbations are small allows the system to be linearized, yielding the following set of equations:

$$\frac{\partial u}{\partial t} + U\frac{\partial u}{\partial x} + V\frac{\partial u}{\partial y} + w\frac{\partial U}{\partial z} - fv = -\frac{1}{\rho}\frac{\partial p}{\partial x} + \nu\nabla^2 u,$$
$$\frac{\partial v}{\partial t} + U\frac{\partial v}{\partial x} + V\frac{\partial v}{\partial y} + w\frac{\partial V}{\partial z} + fu = -\frac{1}{\rho}\frac{\partial p}{\partial y} + \nu\nabla^2 v,$$
$$\frac{\partial w}{\partial t} + U\frac{\partial w}{\partial x} + V\frac{\partial w}{\partial y} = -\frac{1}{\rho}\frac{\partial p}{\partial z} + \nu\nabla^2 w,$$
$$\frac{\partial u}{\partial x} + \frac{\partial v}{\partial y} + \frac{\partial w}{\partial z} = 0. \qquad (2)$$

The perturbations are assumed to be of the form

$$u(x, y, z, t) = \hat{u}(z)\exp[i(\alpha x + \gamma y - \omega t)].$$

The x and y components of the wavenumber vector are α and γ, respectively, and ω is the complex frequency.

The coordinate system is now rotated. This is accomplished through the use of the following transformations.

$$\tilde{\alpha}\tilde{u} = \gamma\hat{u} - \alpha\hat{v}, \quad \tilde{\alpha}\tilde{U} = \gamma U - \alpha V,$$
$$\tilde{\alpha}\tilde{v} = \alpha\hat{u} + \gamma\hat{v}, \quad \tilde{\alpha}\tilde{V} = \alpha U + \gamma V,$$
$$\tilde{\alpha}^2 = \alpha^2 + \gamma^2.$$

The perturbation velocity components parallel to and perpendicular to the disturbance wavefront are $\tilde{u}$ and $\tilde{v}$, respectively. Since α and γ are the x and y components of the wavenumber vector, $\tilde{\alpha}$ is the magnitude of that vector.

The perturbation equations can be written as the following sixth-order system of ordinary differential equations.

$$[\nabla^2 - i\tilde{\alpha}\,\mathrm{Re}(\tilde{V} - c)](i\tilde{\alpha}\tilde{u}) = i\tilde{\alpha}\,\mathrm{Re}\tilde{U}'\hat{w} + 2\hat{w}', \quad (3a)$$
$$[\nabla^2 - i\tilde{\alpha}\,\mathrm{Re}(\tilde{V} - c)]\nabla^2\hat{w} + i\tilde{\alpha}\,\mathrm{Re}\tilde{V}''\hat{w} = -2i\tilde{\alpha}\tilde{u}', \quad (3b)$$

where $\omega = \tilde{\alpha}c$. The equations have been nondimensionalized on the velocity scale U_s, the length scale δ, and the time scale δ/U_s. The Reynolds number is $\mathrm{Re} = U_s\delta/\nu$. Primes denote differentiation with respect to z.

b. Boundary conditions and method of solution

For the perturbations in an Ekman layer bounded by a rigid surface, the appropriate boundary conditions are

$$\tilde{u} = \tilde{v} = \hat{w} = 0 \quad \text{as} \quad z \to -\infty,$$
$$\tilde{u} = \tilde{v} = \hat{w} = 0 \quad \text{at} \quad z = 0.$$

For the case of a free surface Ekman layer, the conditions as $z \to -\infty$ are the same. Those at $z = 0$ are different, however. The proper conditions on the horizontal perturbation components are that they exert no stress at the surface:

$$\frac{\partial\tilde{u}}{\partial z} = \frac{\partial\tilde{v}}{\partial z} = 0 \quad \text{at} \quad z = 0.$$

The third boundary condition is a consequence of the fact that the pressure is a constant at the free surface (Yih, 1969).

This third condition may be transformed into a condition on $\hat{w}$ and $\tilde{u}$. Let the displacement of the free surface be

$$\eta = \hat{\eta}\exp[i(\alpha x + \gamma y - \omega t)].$$

The pressure condition states that the total pressure is a constant at the surface. The total pressure, however, is the sum of the perturbation pressure p and the pressure which results from the displacement of the surface, $-g\rho\eta$, where g is the acceleration of gravity. The pressure condition becomes

$$\left.\begin{aligned} &\hat{p} - g\hat{\eta} = 0 \quad \text{at} \quad z = 0 \\ \text{where} \quad &p/\rho = \hat{p}(z)\exp[i(\alpha x + \gamma y - \omega t)] \end{aligned}\right\}. \qquad (4)$$

The equations of motion may be used to obtain $\hat{p}$ in terms of $\hat{w}$, $\tilde{u}$, and their derivatives. Additionally, the surface displacement is related to the vertical perturbation velocity by the equation

$$w = \frac{D\eta}{Dt} \quad \text{at} \quad z = 0.$$

Substitution of these forms of the pressure and displacement into (4) yields the third boundary condition for the problem. The boundary conditions for a free surface Ekman layer then become

$$\tilde{u} = \tilde{v} = \hat{w} = 0 \quad \text{as} \quad z \to -\infty, \tag{5a}$$

$$\frac{\partial \tilde{u}}{\partial z} = \frac{\partial \tilde{v}}{\partial z} = 0 \quad \text{at} \quad z = 0, \tag{5b}$$

$$[-\mathrm{Re}\tilde{\alpha}^2 c^2 + \mathrm{Re}\,\mathrm{Fr}\tilde{\alpha} + (\tilde{V} - c)(\tilde{\alpha}\,\mathrm{Re}\tilde{V}')]\hat{w} + (\tilde{V} - c)[-\mathrm{Re}\tilde{\alpha}(\tilde{V} - c) + i\tilde{\alpha}^2 + 2i\tilde{\alpha}]\hat{w}' + [-i(\tilde{V} - c)]\hat{w}''' + [2\tilde{\alpha}(\tilde{V} - c)]\tilde{u} = 0 \quad \text{at} \quad z = 0, \tag{5c}$$

where $\mathrm{Fr} = g\delta/U_s^2$.

The boundary conditions (5) along with (3) form an eigenvalue problem in which Re, α, γ, and Fr are held fixed and the eigenvalue c determined. This was accomplished by means of a standard shooting technique.

Since (3) is a sixth-order system, there will exist six independent solutions. Far from the free surface, the coefficients of (3) are constant, and exact solutions in the form of exponentials can be found. Examination of the form of (3) reveals that the six roots of the characteristic equation consist of six complex numbers, three with positive and three with negative real parts. Elimination of the three solutions represented by roots with negative real parts satisfies (5a). The three remaining solutions were used to provide starting values for a fourth order Runge–Kutta integration scheme. A guess was made for c, and the three independent solutions were integrated in to $z = 0$. At $z = 0$, it was determined by how much the calculated solutions missed fitting the remaining boundary conditions, (5b) and (5c). The secant method was employed to find the value of c which provided a satisfactory small value of this residue. The range of integration was $-10 \leqslant z \leqslant 0$, the step size $\Delta z = 0.2$, and the convergence criterion was that the change in $|c|$ between successive estimates was less than 10^{-5} (for details, see Appendix).

c. *Effect of boundary conditions on the eigenvalues*

The boundary condition (5c) contains the parameter $\mathrm{Fr} = g\delta/U_s^2$. For oceanic parameters this number is very large. For example, a surface velocity of 0.2 m s^{-1}, and a scaling depth $\delta = 12$ m yields $\mathrm{Fr} \sim 3.3 \times 10^3$. In view of the size of this parameter, it is natural to question the importance of the remaining terms in (5c). Eigenvalues were obtained at three different Reynolds numbers for a series of Fr values. The wavenumbers in these examples were chosen to correspond to regions of anticipated maximum growth rates, based on the work of Faller and Kaylor (1967) and Lilly (1966). Growth rate is defined as $\omega = \tilde{\alpha}c$. The results are shown in Fig. 1, where disturbance growth rates are plotted against Fr^{-1}. Examination of the figure leads to the not surprising conclusion that in the range of interest for geophysical problems, $\mathrm{Fr}^{-1} \ll 1$, an excellent approximation to the solution may be obtained by retaining only the term multiplied by Fr in (5c). The boundary conditions become, then,

$$\tilde{u} = \tilde{v} = \hat{w} = 0 \quad \text{as} \quad z \to -\infty, \tag{6a}$$

$$\frac{\partial \tilde{u}}{\partial z} = \frac{\partial \tilde{v}}{\partial z} = \hat{w} = 0 \quad \text{at} \quad z = 0. \tag{6b}$$

These will be referred to as the boundary conditions for a free surface problem.

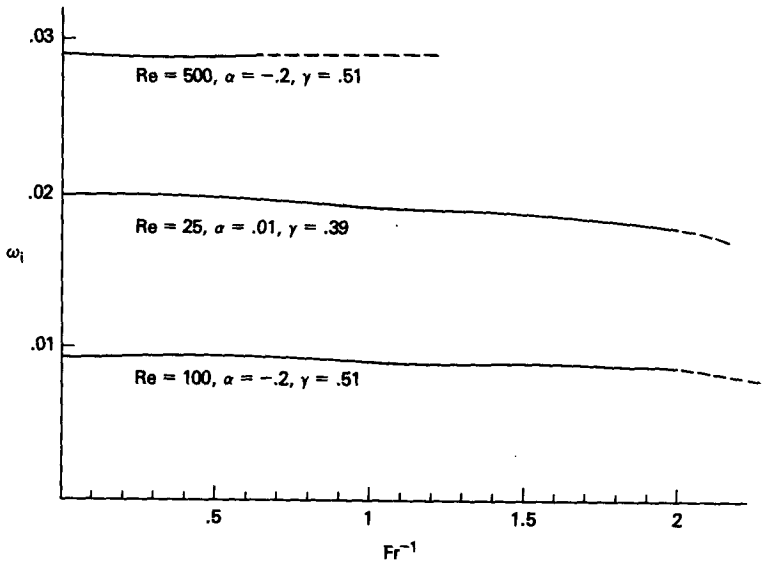

FIG. 1. Plot of growth rate ω_i as a function of Fr^{-1} for three different Reynolds numbers: Re = 25, $\alpha = 0.01$, $\gamma = 0.39$; Re = 100, $\alpha = -0.2$, $\gamma = 0.51$; Re = 500, $\alpha = -0.2$, $\gamma = 0.51$.

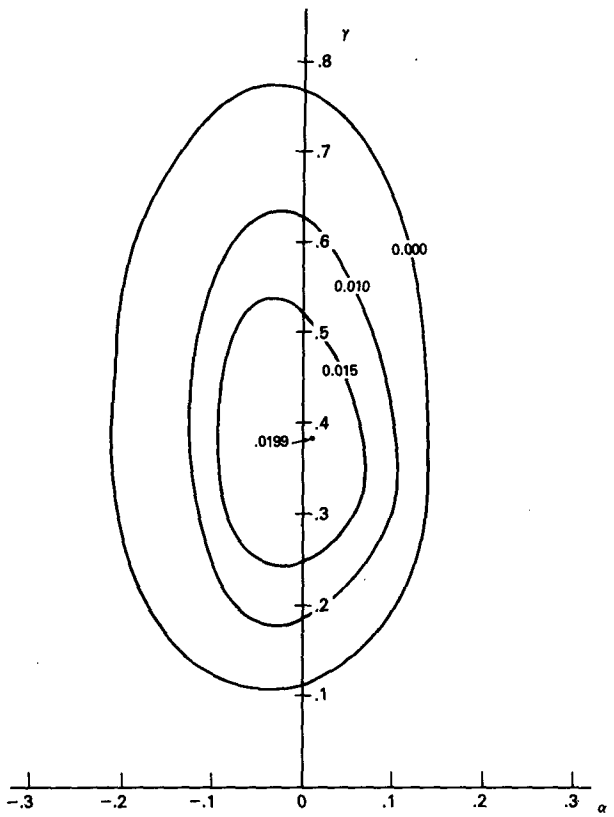

FIG. 2. Contours of growth rate ω_i as a function of wavenumber for Re = 25.

d. Results for the homogeneous case

Figs. 2, 3 and 4 show contour plots of growth rate as a function of α and γ for Reynolds numbers of 25, 65 and 100, respectively. The plot for Re = 25 is very similar to the one produced by Faller and Kaylor (1967). There is a maximum growth rate located at $\alpha = 0.01$, $\gamma = 0.39$. If this extremum is traced back through Reynolds number space, a critical Reynolds number of 11.647 is found at the location $\alpha = 0.05$, $\gamma = 0.33$. This is in good agreement with the Faller and Kaylor (1967) estimated critical Reynolds number of 12 ± 3 and the value of Re = 11.816 obtained with bifurcation methods by Iooss *et al.* (1978). The nondimensional phase speed of the mode at the critical Reynolds number is estimated as $c_r = -0.527$. This departs somewhat from the results of Iooss *et al.* (1978) who obtained a value of −0.561. There is also a slight difference in the location of the extremum in wavenumber space. Iooss *et al.* located the critical mode at $\alpha = 0.034$, $\gamma = 0.318$. It should be noted, however, that the numerical method employed in this work is much less sophisticated than that of Iooss *et al.*, and this may account for the difference in results.

In Fig. 3, the growth rate contours have not altered markedly from those in Fig. 2. There is a slight shift in the location of the maximum growth rate. It is now located at $\alpha = -0.04$, $\gamma = 0.31$. In general, however, the isopleth pattern remains the same.

At Re = 100, however, the situation changes, as shown in Fig. 4. Whereas previously there was a single maximum in growth rate, two now exist. In itself, this is not a surprising result. It is, in fact, expected, as this is what occurs in the stability problem for a rigid boundary Ekman layer. In this case, however, it appears that the two different unstable modes can exist simultaneously for certain pairs of wavenumbers. Lilly (1966) pointed out that for the rigid boundary Ekman layer, no more than one unstable eigenvalue was ever found for a given set of parameters. It appears that this is not necessarily true for the free surface case.

In the rigid boundary case, the two types of instability present are the parallel mode and the inflection point mode, as demonstrated by Lilly. The parallel mode is dependent upon the mean component of shear parallel to its wavefront as a source of energy, whereas the inflection point mode draws upon the shear in the mean velocity component perpendicular to its wavefront and requires the presence of an inflection point in that velocity component.

Several numerical experiments were run to determine the types of instabilities occurring in the present case. Arbitrarily setting the component of shear par-

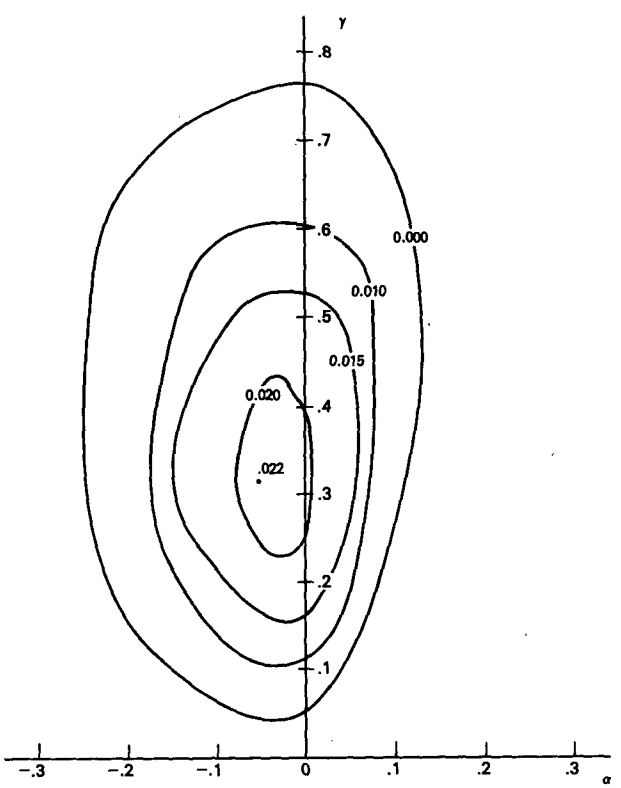

FIG. 3. As in Fig. 2, but for Re = 65.

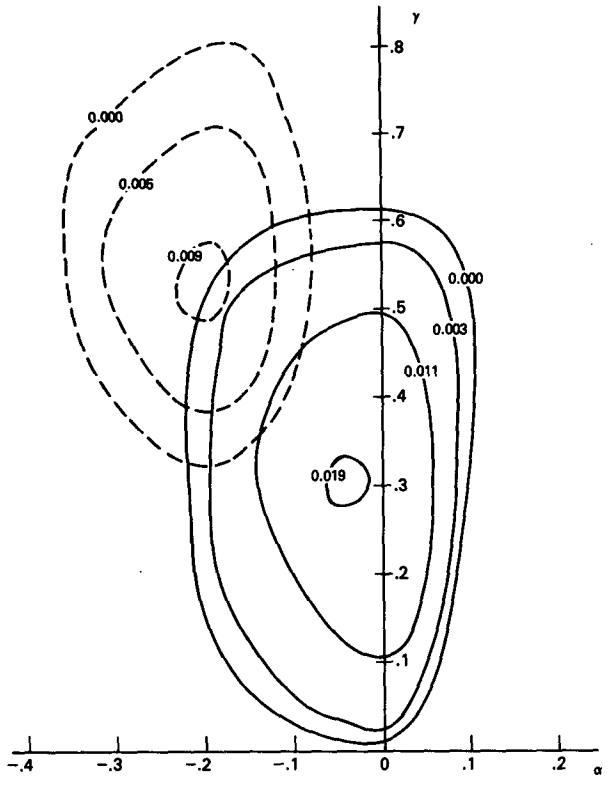

FIG. 4. As in Fig. 2, but for Re = 100.

allel to the disturbance wavefront equal to zero had little effect on the growth rate of the mode centered at $\alpha = -0.20$, $\gamma = 0.53$. Smoothing the velocity component perpendicular to the wavefront and thereby removing its inflection points, however, stabilized this mode. It seems safe to assume that this is an inflection point mode. The mode centered near $\alpha = -0.04$, $\gamma = 0.31$ was stabilized by removal of the parallel component of shear, but remained unstable when inflection points were removed. This, then, seems to be a parallel mode of instability. As in the rigid boundary case, there are two types of instability present. The locations of the extrema associated with these modes are somewhat different, however.

In the rigid boundary case, the inflection point mode is centered near $\alpha = -0.10$, $\gamma = 0.51$ and the parallel mode near $\alpha = 0.04$, $\gamma = 0.30$ (Lilly, 1966). Thus, in the free surface case the inflection point extremum occurs at a somewhat larger wavenumber than (and oriented $\sim 10°$ counterclockwise from) the rigid boundary case. The wavenumber vector of the parallel extremum has approximately the same magnitudes in the two cases, but that of the free surface case is rotated approximately 14° counterclockwise from the rigid boundary case.

Phase speeds for the parallel mode and the inflection point mode extrema are $c_r = -0.319$ and $c_r = -0.278$, respectively.

Unfortunately, it proved difficult to track the contours of the separate modes at higher Reynolds numbers. By analogy with the rigid boundary case, one would expect that at higher Reynolds numbers the inflection point mode would tend to dominate and the parallel mode to eventually disappear. There is evidence, however, that this is not accomplished in the present case by the simple disappearance of the parallel mode along with the expansion of the inflection point mode. Whereas the two modes possess separate "sheets" in eigenvalue space at Re = 100, at higher Reynolds numbers it appears that these sheets fuse to form a single surface of unstable eigenvalues as is found in the rigid boundary case.

Evidence for this process can be seen in Figs. 5 and 6. These portray phase speeds and growth rates along a line of fixed γ which intersects both eigenvalue

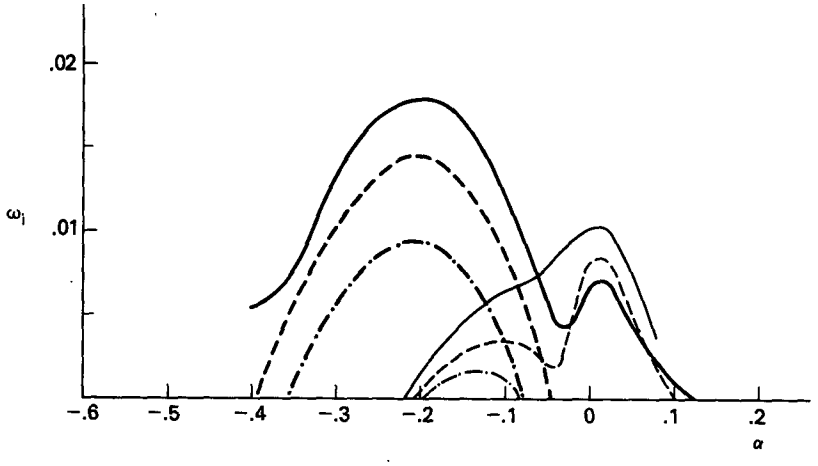

FIG. 5. Growth rates ω_i, for fixed $\gamma = 0.51$ [solid line, parallel mode, Re = 100; heavy dash-dot line, inflection point mode, Re = 100; dashed line, parallel mode, Re = 120; heavy dashed line, inflection point mode, Re = 120; dash-dot line, parallel mode, Re = 140; heavy solid line, inflection point mode, Re = 140].

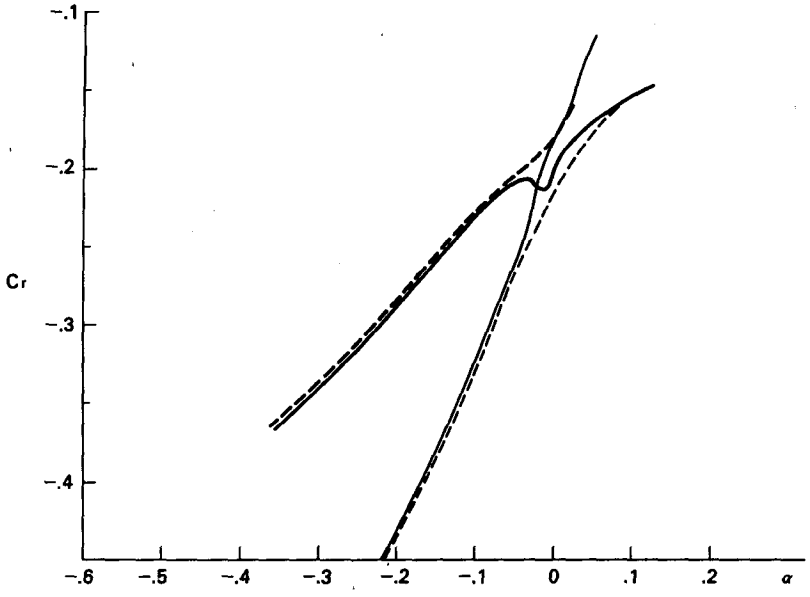

FIG. 6. Phase speed c_r for fixed $\gamma = 0.51$ [dashed line, parallel mode, Re = 100; heavy dashed line, inflection point mode, Re = 100; solid line, parallel mode, Re = 130; heavy solid line, inflection point mode, Re = 130].

modes at Re = 100. The joining of the separate eigenvalue surfaces can clearly be traced as Re increases.

Fig. 7 is a plot of the eigenfunctions $\hat{w}$, for the two different modes at Re = 100, $\alpha = -0.12$, $\alpha = 0.51$. Although the two modes have distinct eigenvalues ($\omega_r = 0.1845$, $\omega_i = 0.0057$ for the parallel mode, and $\omega_r = 0.1259$, $\omega_i = 0.0053$ for the inflection point mode), the real part of their eigenfunctions are very similar. The imaginary parts differ more markedly, with the inflection point mode having a smaller amplitude and changing sign earlier than the parallel mode.

A comparison of the eigenfunctions for the rigid boundary case and the free surface case is shown for a Reynolds number of 65 in Figs. 8, 9, 10, and 11. Although the free boundary conditions do not appear to produce much effect on the vertical perturbation velocity, there is a notable difference in the horizontal components.

Finally, Fig. 12 is a plot of the growth rate associated with the inflection point extremum.

3. The two-layer case

Next, the stability of an Ekman layer in a two layer system will be examined. A top layer of finite depth and density ρ is assumed to exist above a bottom layer of density ρ^* and infinite depth. Fig. 13 depicts the physical situation. This problem differs from the homogeneous case in two ways. First, the presence of a density interface, along with an attendant change in eddy viscosity, will alter the mean Ekman flow and confine it to the upper layer. Second, when perturbations develop in the upper layer, the density interface will tend to inhibit penetration of cells into the lower layer.

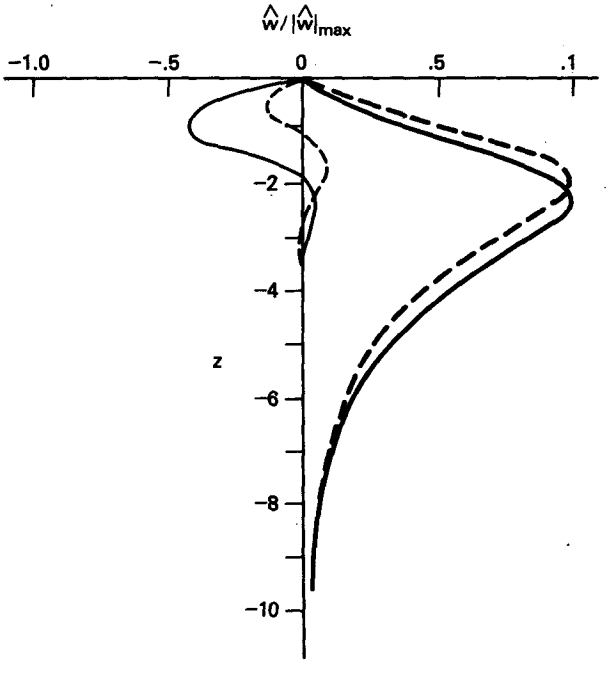

FIG. 7. Normalized vertical perturbation velocity $\hat{w}/|\hat{w}|_{max}$, for Re = 100, $\alpha = -0.12$, $\gamma = 0.51$ [heavy solid line, Real $(\hat{w}/|\hat{w}|_{max})$, parallel mode; solid line, Imaginary $(\hat{w}/|\hat{w}|_{max})$, parallel mode; heavy dashed line, Real $(\hat{w}/|\hat{w}|_{max})$, inflection point mode; dashed line, Imaginary $(\hat{w}/|\hat{w}|_{max})$, inflection point mode].

a. The mean flow

The problem of Ekman flow in a two layer fluid has been considered by Nomitsu (1933). Although the mean equations of motion are the same as those in the homogeneous case, the boundary conditions differ. While the upper and lower layers are regarded as having a constant eddy viscosity, at a sharp density interface the eddy viscosity may fall to almost zero, thus confining the effect of the wind to the top layer (Defant, 1961). At the interface, since the water will meet no resistance, it is assumed that the lighter top layer of fluid will slide over the heavier lower layer with no transmission stress. The boundary conditions for the mean flow in the top layer are

$$U = U_s, \quad V = 0 \quad \text{at} \quad z = 0,$$

$$\frac{\partial U}{\partial z} = \frac{\partial V}{\partial z} = 0 \qquad \text{at} \quad z = -h.$$

The nondimensional solution for the mean velocity in the top layer can be written as

$$U = (C_1 \cos z - C_2 \sin z)e^z + [(1 - C_1)\cos z - C_2 \sin z]e^{-z},$$

$$V = (C_1 \sin z + C_2 \cos z)e^z + [-(1 - C_1)\sin z - C_2 \cos z]e^{-z},$$

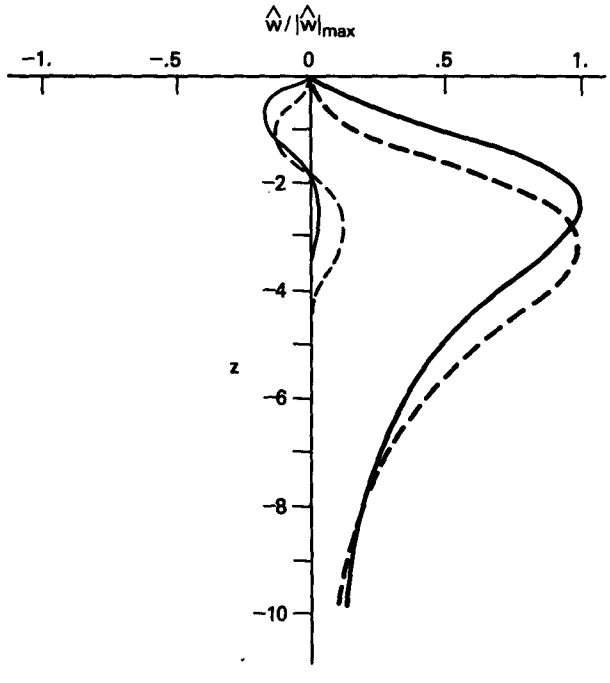

FIG. 8. Normalized vertical perturbation velocity $\hat{w}/|\hat{w}|_{max}$, for Re = 65, $\alpha = -0.04$, $\gamma = 0.33$ [heavy solid line, Real ($\hat{w}/|\hat{w}|_{max}$), free boundary; solid line, Imaginary ($\hat{w}/|\hat{w}|_{max}$), free boundary; heavy dashed line, Real ($\hat{w}/|\hat{w}|_{max}$), rigid boundary; dashed line, Imaginary ($\hat{w}/|\hat{w}|_{max}$), rigid boundary].

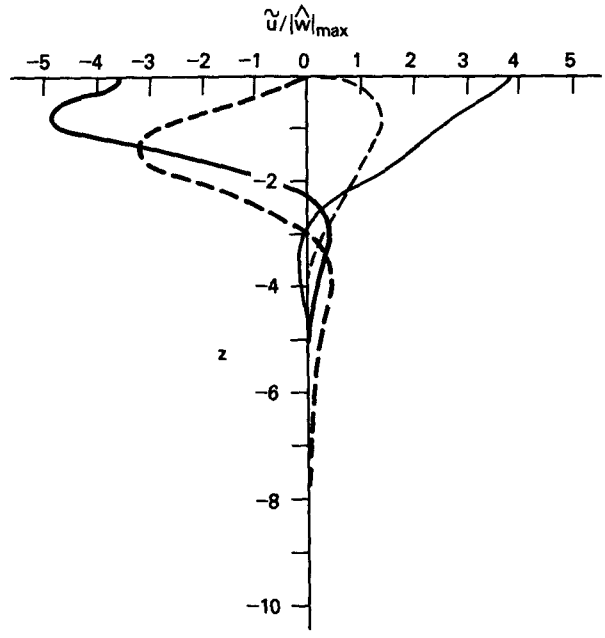

FIG. 9. Normalized horizontal perturbation velocity $\tilde{u}/|\hat{w}|_{max}$, for Re = 65, $\alpha = -0.04$, $\gamma = 0.33$ [heavy solid line, Real ($\tilde{u}/|\hat{w}|_{max}$), free boundary; solid line, Imaginary ($\tilde{u}/|\hat{w}|_{max}$), free boundary; heavy dashed line, Real ($\tilde{u}/|\hat{w}|_{max}$, rigid boundary; dashed line, Imaginary ($\tilde{u}/|\hat{w}|_{max}$, rigid boundary].

where

$$C_1 = \frac{\exp(2h) + \cos(2h)}{\exp(2h) + \exp(-2h) + 2\cos(2h)},$$

$$C_2 = \frac{\sin(2h)}{\exp(2h) + \exp(-2h) + 2\cos(2h)}.$$

The mean velocity in the lower layer is assumed to be zero.

b. The eigenvalue problem and method of solution

Considered separately, the top and bottom layers are homogeneous fluids. The disturbances in each layer are governed by (3) and require six boundary conditions. Thus, 12 boundary conditions are required in all. Perturbation quantities are defined as in the homogeneous case. In the following discussions, starred and unstarred quantities refer to the bottom and the top layer, respectively.

Far from the free surface, the appropriate conditions are

$$\tilde{u}^* = \tilde{v}^* = \hat{w}^* \to 0 \quad \text{as} \quad z \to -\infty.$$

The free surface boundary conditions are

$$\tilde{u}' = \tilde{v}' = \hat{w} = 0 \quad \text{at} \quad z = 0.$$

The conditions on the horizontal velocities at the boundary between the two layers are the same as those applied to the mean flow, *i.e.*, no transmission of tangential stress.

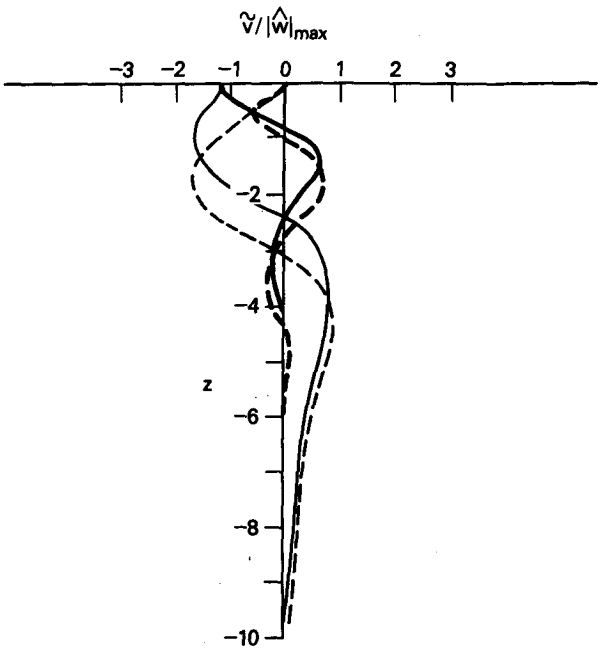

FIG. 10. Normalized horizontal perturbation velocity $\tilde{v}/|\hat{w}|_{max}$, for Re = 65, $\alpha = -0.04$, $\gamma = 0.33$ [heavy solid line, Real $(\tilde{v}/|\hat{w}|_{max})$, free boundary; solid line, Imaginary $(\tilde{v}/|\hat{w}|_{max})$, free boundary; heavy dashed line, Real $(\tilde{v}/|\hat{w}|_{max})$, rigid boundary; dashed line, Imaginary $(\tilde{v}/|\hat{w}|_{max})$, rigid boundary].

$$\tilde{u}' = \tilde{v}' = \tilde{u}^{*\prime} = \tilde{v}^{*\prime} = 0 \quad \text{at} \quad z = -h.$$

Two more conditions are required. The first is obtained by applying the kinematic boundary condition to both sides of the interface. This yields

$$\hat{w} = (1 - \tilde{V}/c)\hat{w}^* \quad \text{at} \quad z = -h.$$

The final condition is a result of the assumption that there is no pressure difference across the interface (Yih, 1969). In dimensional quantities, the pressure condition is

$$p = p^* - g(\rho^* - \rho)\eta,$$

where η is the displacement of the interface and g is the acceleration of gravity. Nondimensionalized and written in terms of the perturbation velocity components, this condition becomes

$$[-\tilde{\alpha}\,\mathrm{Re}(\tilde{V} - c)\hat{w}' + \tilde{\alpha}\,\mathrm{Re}\tilde{V}'\hat{w} + 2\tilde{\alpha}\tilde{u} - i(\hat{w}''' - \tilde{\alpha}^2\hat{w}')] - [\tilde{\alpha}\,\mathrm{Re}c\hat{w}^{*\prime} + 2\tilde{\alpha}\tilde{u}^* - i(\hat{w}^{*'''} - \tilde{\alpha}^2\hat{w}^{*\prime}) + \mathrm{Re}\tilde{\alpha}^2\,\mathrm{Fr}^*\hat{w}^*\omega^{-1} = 0,$$

where $\mathrm{Fr}^* = g\delta(\rho^* - \rho)/(U_s^2\rho)$, and it has been assumed that $\rho^*/\rho \approx 1$.

With these boundary conditions, the perturbation equations can be solved to find the relevant eigenvalues. Once again, Re, α, γ and Fr* were held fixed and the eigenvalue c was searched for with a shooting technique.

In the bottom layer, the coefficients of the perturbation equation are constant, so exact solutions can be found in the form of six exponentials. As in the homogeneous case discussed previously, three of these exponential solutions will grow as $z \to -\infty$ and are therefore eliminated.

In the top layer, there again exist six independent solutions. These may be obtained by integrating the perturbation equations from $z = 0$ to $z = -h$ with appropriate starting conditions. These starting conditions are chosen such that the six solutions satisfy the free surface boundary conditions and are independent.

A guess was made for c, the solutions in the bottom layer calculated analytically, and those in the top layer integrated from $z = 0$ to $z = -h$. It was then determined by how much the calculated solutions missed fitting the boundary conditions at $z = -h$. As in the homogeneous case, an acceptable value of c was found by means of the secant method, an integration step size of $\Delta z = 0.2$ was used, and the convergence criterion was that successive estimates for $|c|$ differed by less than 10^{-5}.

c. *Results for the two layer case*

Fig. 14 is a plot of contours of ω_i as a function of the wavenumbers α and γ. The Reynolds number is 100, $h = -4$, and Fr* = 35. If $U_s = 0.083$ m s^{-1} and $\delta = 12$ m, the ratio $(\rho^* - \rho)/\rho$ has a value of ~0.002

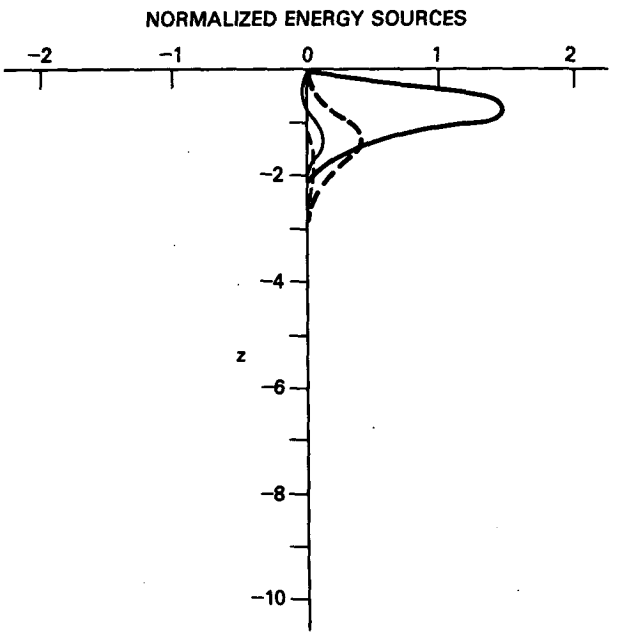

FIG. 11. Normalized energy source terms for Re = 65, $\alpha = -0.04$, $\gamma = 0.31$ [heavy solid line, $-\overline{\tilde{u}\hat{w}}\tilde{U}'/(|\hat{w}|_{max})^2$, free boundary; solid line, $-\overline{\tilde{v}\hat{w}}\tilde{V}'/(|\hat{w}|_{max})^2$, free boundary; heavy dashed line, $-\overline{\tilde{u}\hat{w}}\tilde{U}'/(|\hat{w}|_{max})^2$, rigid boundary; dashed line, $-\overline{\tilde{v}\hat{w}}\tilde{V}'/(|\hat{w}|_{max})^2$, rigid boundary].

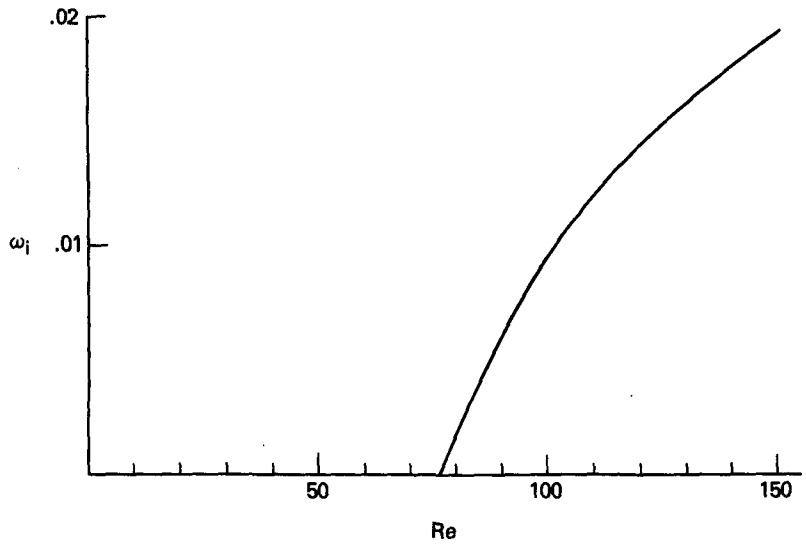

FIG. 12. Growth rate ω_i, as a function of Reynolds number for the inflection point mode ($\alpha = -0.20$, $\gamma = 0.51$).

for this choice of Fr*. The contours are very similar to those shown in Fig. 4 for the homogeneous case. Both the inflection point and the parallel modes are present and are located in approximately the same region of wavenumber space. A detailed search for the maximum growth rates was not made. The calculations which were carried out indicate that the inflection point mode is centered near $\alpha = -0.2$, $\gamma = 0.53$, and that the parallel mode is centered near $\alpha = -0.01$, $\gamma = 0.31$.

The Reynolds number dependence of these modes is shown in Fig. 15. Once again, Fr* = 35 and $h = 4$. The wavenumber values are chosen to correspond to the extrema of Fig. 14, and these growth rates are traced as functions of Reynolds number. It can be seen that the critical Reynolds number is ~90 for the inflection point mode and ~19 for the parallel mode. For both modes, the critical Reynolds number is greater than it is for the homogeneous case. Although this plot shows the parallel mode stabilizing at Re $\approx$ 240, the extremum shifts to a different region of wavenumber space at higher Reynolds numbers, and, in fact, does not stabilize until approximately Re = 420.

The variation of growth rate with the depth of the top layer is shown in Fig. 16. Both modes stabilize as the depth decreases, with the inflection point mode stabilizing first. When h is greater than 6, both modes have eigenvalues nearly identical to those for the homogeneous case.

It should be noted that changing the depth of the top layer has a dual effect. First, it changes the position of the density interface. Second, it affects the mean velocity profile. An effort was made to separate these two effects by making calculations identical to the ones shown in Fig. 16, but with the density dif-

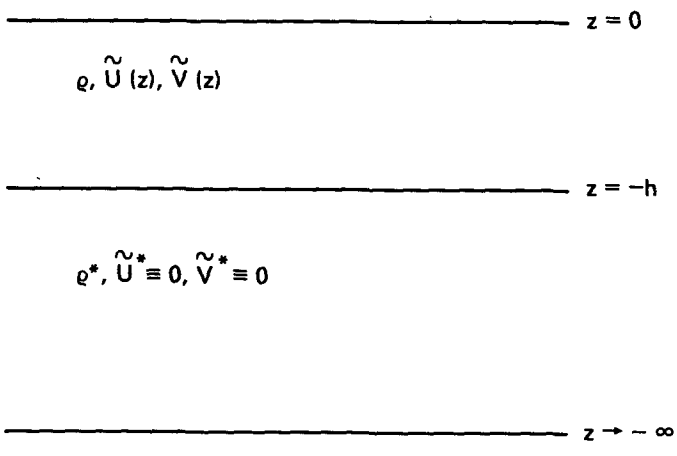

FIG. 13. Physical situation for the two-layer case.

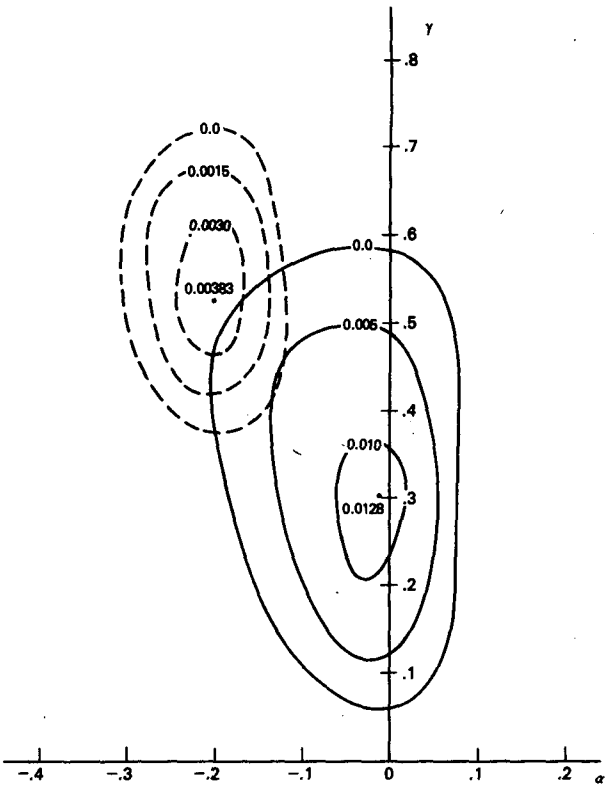

FIG. 14. Contours of growth rate ω_i, as a function of wavenumber for the two layer case (Re = 100, Fr* = 35, h = 4).

ference between the two layers arbitrarily set to zero. The results are shown in Fig. 17.

In this case, the eigenvalues remain very close to those of the homogeneous case until $h \approx 4$. Then there is a slight increase in the growth rate for both modes, followed by a rapid stabilization. The parallel mode stabilizes at approximately the same value of h as in the Fr* = 35 case, but the inflection point mode remains unstable until a smaller value of h is reached.

The behavior of the eigenvalues with changing Fr* is interesting. This behavior is shown in Fig. 18 for Re = 100, h = 4. At Fr* = 0, the eigenvalues are very close to those of the homogeneous case. These values fall rapidly and become stable at very low values of Fr*. For Fr* slightly greater than zero, however, two more modes appear, and the growth rates of these modes rapidly increase to values which are nearly constant with Fr*. Fig. 19 is a plot of the growth rates associated with this second pair of modes. Examination of the values of Fr* = 35 and comparison with Figs. 14 and 4 show that these two modes are still associated with the parallel and inflection point instability.

Finally, Fig. 20 is a plot of the eigenfunctions of the disturbance associated with the parallel mode. Both the mode which stabilizes as Fr* increases, and that which destabilizes as Fr* increases are shown.

4. Discussion

a. The homogeneous case

Perhaps the most notable difference between the growth rates of this case and those of a homogeneous rigid boundary case (henceforth referred to as simply the rigid boundary case) is that the free boundary problem becomes unstable at a much lower Reynolds number. As in the rigid boundary problem, the mode which becomes unstable first is the parallel mode. The critical Reynolds number for the inflection point

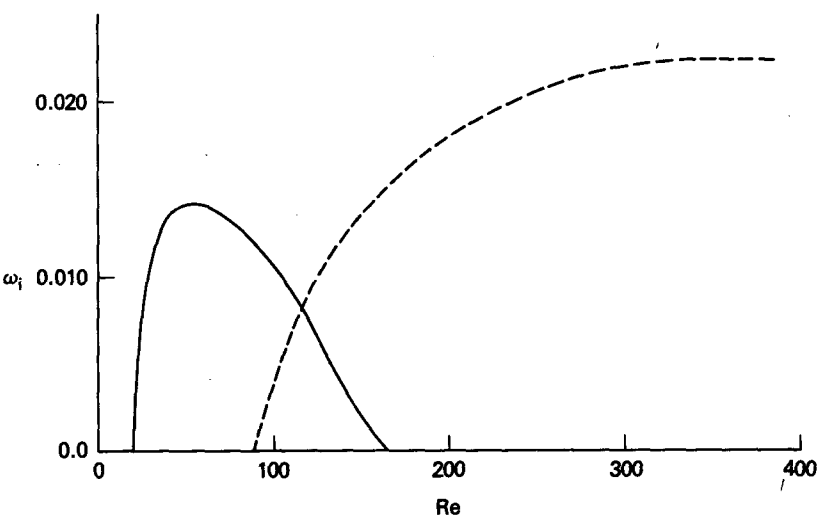

FIG. 15. Growth rate ω_i, as a function of Reynolds number for the two-layer case [heavy solid line, parallel mode, α = −0.04, γ = 0.31, Fr* = 35, h = 4; heavy dashed line, inflection point mode, α = 0.20, γ = −0.51, Fr* = 35, h = 4].

made is also lower, as is seen in Fig. 12. This mode becomes unstable at a Reynolds number of approximately 75, as compared to ~115 in the rigid boundary case.

Examination of Fig. 11 reveals a possible candidate for the source of this difference. The energy available to the perturbation through the source terms $-\tilde{u}\hat{w}\tilde{U}'$ and $-\tilde{v}\hat{w}\tilde{V}'$ is greater in the free surface case. Presumably, this is because the horizontal perturbation velocities are not forced to go to zero at the boundary. Even though $\hat{w}$ still must go to zero at $z = 0$, the net effect of relaxing the conditions on $\tilde{u}$ and $\tilde{v}$ is to allow the existence of larger Reynolds stresses. These occur in the region where the mean shear is greatest, and the result is a more efficient extraction of energy from the mean flow.

The coexistence of more than one unstable mode for a given set of parameters α, γ and Re presents a problem more difficult to explain. Possibly the existence of distinct modes is allowed in this case because there is enough energy available to support each one separately. This does not explain however, why the parallel mode does not simply disappear with increasing Reynolds number instead of apparently merging into the sheet corresponding to the inflection point mode. The subtleties of this process remain unresolved.

The double mode structure has certain implications for the initial value problem in an Ekman layer. The similarity of the two modes' eigenfunctions, demonstrated in Fig. 7, suggests that, if one mode is excited by an initial disturbance, both may be. The resulting perturbation, which is the sum of the two separate modes, might well appear to be a single wave

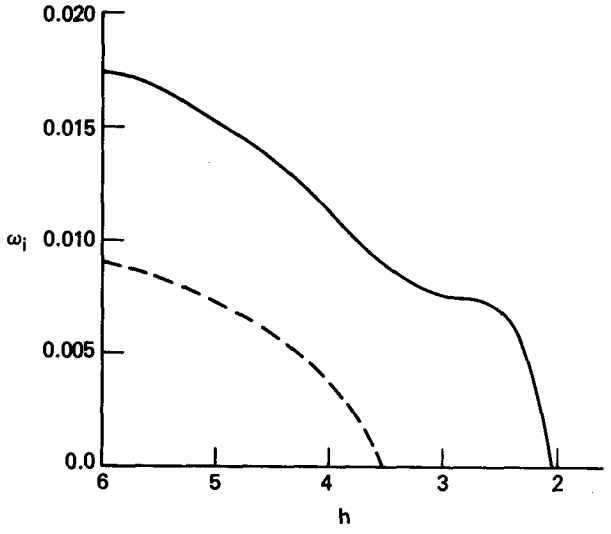

FIG. 16. Growth rate ω_i, as a function of h for the two-layer case [heavy solid line, parallel mode, $\alpha = -0.04$, $\gamma = 0.31$, Re = 100, Fr* = 35; heavy dashed line, inflection point mode, $\alpha = -0.20$, $\gamma = -0.51$, Re = 100, Fr* = 35].

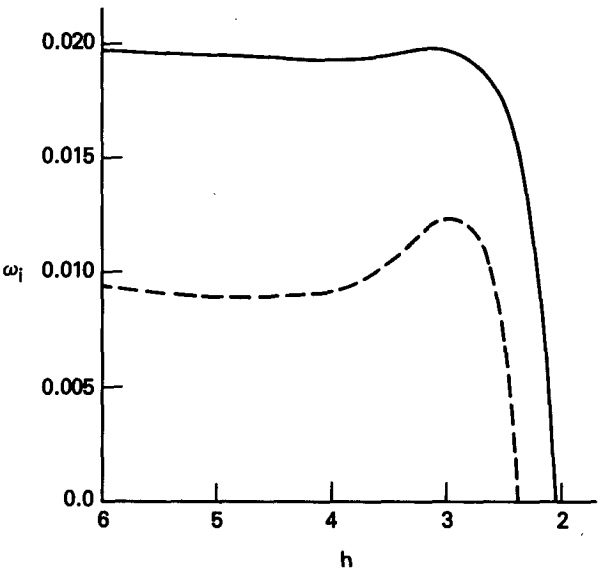

FIG. 17. Growth rate ω_i, as a function of h for the two-layer case [heavy solid line, parallel mode, $\alpha = 0.04$, $\gamma = 0.31$, Re = 100, Fr* = 35; heavy solid line, inflection point mode, $\alpha = -0.20$, $\gamma = 0.51$, Re = 100, Fr* = 35].

since the horizontal wavenumbers are identical. The growth rate of such a disturbance is the sum of the individual growth rates. In the example given in Fig. 7, $\omega_i = 0.00573$ for the parallel mode and $\omega_i = 0.00534$ for the inflection point mode. The wave representing the sum of these two disturbances would have a growth rate very nearly equal to that of the maximum growth rate of the parallel mode and exceeding that of the inflection point mode. The result might be a very broad peak in the power spectrum of an arbitrary disturbance. An initial disturbance might well maintain a compact shape much longer than in the rigid boundary case and take much longer to develop into a well defined wave packet.

Finally, it should be noted that in the free surface case considered here, which is analogous to an oceanic Ekman layer, the most unstable modes both possess phase speeds which are a significant fraction of the speed at the surface. For example, at Re = 100, the parallel mode has a phase speed of −0.319 and the inflection point mode has a phase speed of −0.278. This is in contrast to the rigid boundary, atmospheric type Ekman layer, where the phase speed of the inflection point mode is very close to zero.

However, these differences in phase speeds are, in large part, not a reflection of different physics but of different coordinate systems. If the free surface case is considered in a coordinate system (x', y') whose origin is moving with the surface velocity and is oriented such that the velocity far from the surface is in the x' direction, the perturbation equations will be the same as those for the atmospheric case. To convert the phase speeds of the free surface case into

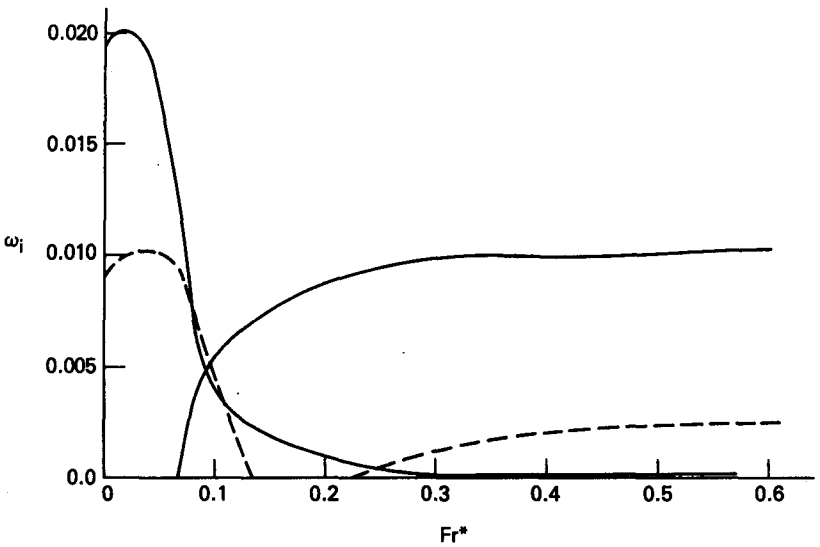

FIG. 18. Growth rate ω_i, as a function of Fr* [heavy solid line, parallel mode, Re = 100, $\alpha = -0.04$, $\gamma = 0.31$, $h = 4$; heavy dashed line, inflection point mode, Re =.100, $\alpha = -0.20$, $\gamma = 0.51$, $h = 4$].

those which will occur in the primed coordinate system, the appropriate transformation is

$$c_r' = c_r - \cos\Phi,$$

where c_r' is the phase speed in the primed coordinate system and $\Phi = \tan^{-1}(\gamma/\alpha)$. With this transformation, the phase speeds of the parallel mode and the inflection point mode become 0.190 and −0.075 respectively, which are much closer to the values which have been obtained for the rigid boundary case.

b. The two-layer case

Examination of Fig. 14 indicates that the two-layer case appears to be more stable than the homogeneous case. Although the growth rates in this example are still greater than those of the rigid boundary case at a comparable Reynolds number, they are less than those shown in Fig. 4. Additionally, the regions of instability in the α–γ plane are smaller for both modes in the two layer case. Further indications of

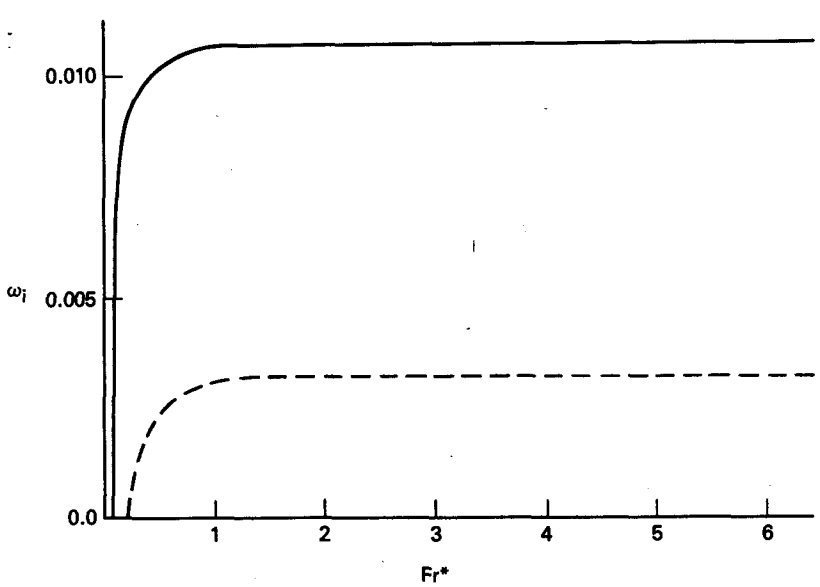

FIG. 19. Growth rate ω_i, as a function of Fr* [heavy solid line, parallel mode, Re = 100, $\alpha = -0.04$, $\gamma = 0.31$, $h = 4$; heavy dashed line, inflection point mode, Re = 100, $\alpha = -0.20$, $\gamma = 0.51$, $h = 4$].

this stabilization are the critical wavenumbers, which are larger than those in the homogeneous case for both modes of instability.

Despite this change in magnitude, the location of the most growing modes in α–γ space has changed very little from what occurs in the homogeneous problem.

Fig. 14 represents a case in which the top layer extends to $z = -4$. This is very nearly the depth of the boundary layer in the homogeneous case, and, correspondingly, there is little difference in the mean velocity profiles for the two cases. Presumably, it is the presence of the density interface which has a damping influence on the instabilities, a conjecture which is supported by examination of Figs. 16 and 17. Without a density interface present, there is little change in the eigenvalues until $h \approx 3.5$. The eigenvalues then actually become slightly more unstable before stabilizing at approximately the same value of h as when there is a density interface present. These results seem to indicate that it is the change in mean velocity profile which causes the ultimate stability cutoff in both modes. The interface, however, has a large effect on the relative magnitude of the growth rate.

It appears as if each physical mode of instability can occur in two different eigenfunction types. These are shown in Fig. 20 for the parallel mode. The first, call it type 1, occurs at low values of Fr* and is similar to the eigenfunctions for the homogeneous problem. In fact, for $h = 4$ and Fr* = 0, the eigenfunctions and eigenvalues differ only slightly from those of the homogeneous case. With increasing Fr* the type 1 eigenfunction is stabilized, and a new eigenfunction, type 2, comes into existence. A very small density difference is enough to accomplish this, and once it occurs, the type 2 eigenvalue remains constant out to large values of Fr*, as shown in Fig. 19. The type 2 eigenfunction is essentially limited to the top layer.

Examination of Fig. 21 reveals a possible explanation for this behavior. The dispersion relation for an inviscid internal wave in a two layer system is

$$c = V_0 \pm \left[\frac{\mathrm{Fr}^*}{\tilde{\alpha}(\coth(\tilde{\alpha}h) + 1)}\right]^{1/2},$$

in the present system of nondimensionalization. The top layer is of depth h, the bottom layer is assumed to be infinitely deep, and V_0 is the mean speed of the fluids.

In Fig. 21, the value of c obtained from this relation using the negative square root and a mean speed of zero is plotted as a function of Fr*. The wavenumbers correspond to the extremum of the parallel mode of instability. Also plotted are the phase speeds of the two types of eigenfunctions discussed above.

Although initially far apart, the curves representing the type 1 eigenfunction and the internal waves converge rapidly and parallel one another for Fr* > 1. If $V_0 = -0.05$, a value obtained if $\tilde{V}$ is integrated over $-11 \lesssim z < 0$ and then averaged, the two curves coincide for Fr* > 1.

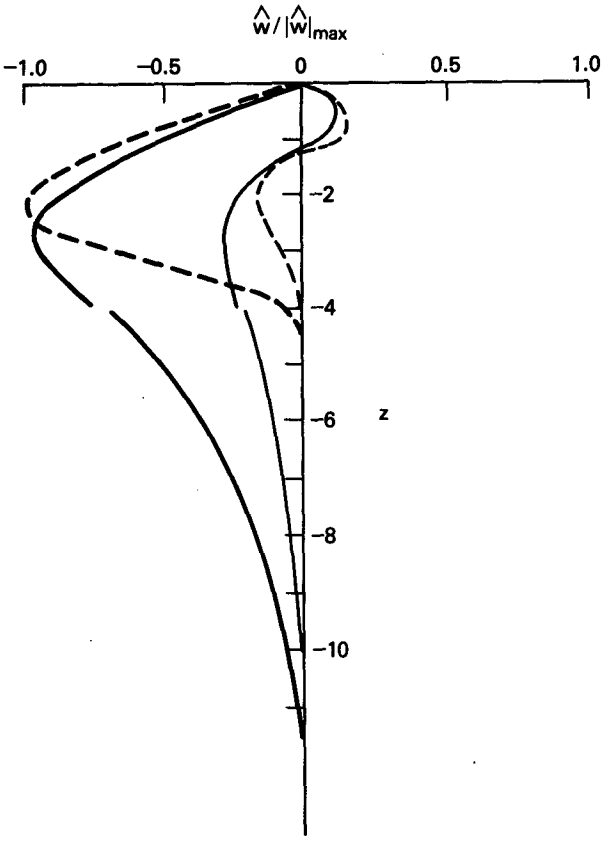

FIG. 20. Normalized vertical perturbation velocity, $\hat{w}/|\hat{w}|_{max}$, for Re = 100, $\alpha = -0.04$, $\gamma = 0.31$, $h = 4$ [heavy solid line, Real ($\hat{w}/|\hat{w}|_{max}$), Fr* = 0; solid line, Imaginary ($\hat{w}/|\hat{w}|_{max}$, Fr* = 0; heavy dashed line, Real ($\hat{w}/|\hat{w}|_{max}$), Fr* = 35; dashed line, Imaginary ($\hat{w}/|\hat{w}|_{max}$), Fr* = 35].

The type 1 eigenfunction has in common with the gravest internal wave mode the property that it has large amplitude near the density interface. It would seem that a very small increase in density stratification causes the type 1 eigenfunction in coalesce with the internal wave mode. In fact, resonance between the two modes may account for the maximum in the growth rate which occurs for the type 1 eigenfunction. Evidence for such a resonance in the continuously stratified case has been reported by Fuller and Kaylor (1967) and Kaylor and Fuller (1972). Increasing stratification eventually stabilizes the mode, however. The energy available from the mean shear is no longer sufficient to displace the density interface, and the type of instability becomes indistinguishable from a damped interval wave (there is dissipation in the system).

As Fr* increases, the shear instability reappears as the type 2 eigenfunction, which is confined to the top

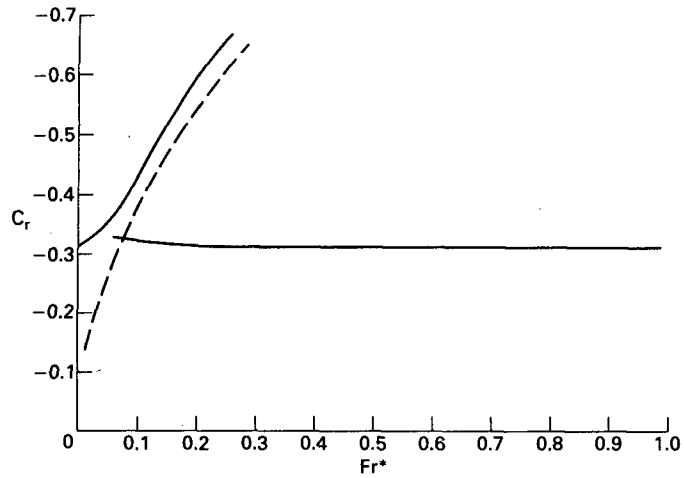

FIG. 21. Phase speed c_r, as a function of Fr* [heavy solid line, parallel mode, Re = 100, $\alpha = -0.04$, $\gamma = 0.31$, $h = 4$; heavy dashed line, internal wave mode, $\alpha = -0.04$, $\gamma = 0.31$, $h = 4$].

layer. Thus it does not have to work to displace the interface. The type 2 disturbance is very similar to what would occur if it had as its lower bound a rigid wall.

Since the density interface functions as a wall in its constraint of the eigenfunction, it might seem reasonable to expect that as h decreases, there would be a shift in the stability contours to larger wavenumbers. Rather surprisingly, this does not seem to occur for the inflection point mode. Even when $h = 4$, which is quite close to the cut off point in Fig. 16, the maximum growth rate remains close to the same location in wavenumber space as in the homogeneous case. In contrast, the parallel mode does seem to exhibit some shift to higher wavenumbers as h decreases. Further calculations at a value of $h = 2.2$ reveal that for Re = 100, Fr* = 35, the maximum growth rate has shifted to the region of $\alpha = -0.08$, $\gamma = 0.45$. There appears to be little change, however, in the cutoff value of h from that depicted in Fig. 16.

It appears that for h less than a value of ~ 2, the parallel and inflection point modes are stable in the two layer case. This would seem to make them unlikely candidates as the stirring agents which act to deepen a preexisting mixed layer. It should be realized, however, that other modes of instability, such as Kelvin–Helmholtz waves, for example, might well occur in such a situation. However, the search for other modes was outside the bounds of the present work.

Acknowledgment. This research was carried out while the author was an NRC/NRL Cooperative Research Associate at the Naval Research Laboratory.

APPENDIX

The Shooting Method

The shooting method is a means by which successive estimates of the eigenvalue c are calculated until the boundary conditions of the problem are satisfied to within an acceptable tolerance. In practice, this amounts to determining the zeros of a function, $f(\alpha, \gamma, \mathrm{Re}, c)$, which is the residue obtained from the difference between the desired values of the boundary conditions and the values obtained by use of the calculated solutions. When α, γ and Re are fixed, f will be an analytic function of the complex eigenvalue c. The secant method of root finding is easily adapted to this case.

Since f is analytic, it can be expanded in a Taylor series about a point c_0 which is close to a root of f. The same arguments which are used to derive Newton's method of root finding for real valued functions then follow directly for the complex case, as do those for the closely related secant method (see, e.g., Hornbeck, 1975). The secant method, which employs a difference expression inplace of the derivative found in Newton's method, was employed here as it was less cumbersome than calculating an approximation for the derivative of f.

Two initial guesses are needed to implement the secant method. The first was made with the aid of previously published work (Faller and Kaylor, 1967) or calculations made previously in the area of interest. The second guess was made at a point $c_0 + \Delta c$ where $|\Delta c| = 10^{-4}$.

TABLE 1. Eigenvalues c, and growth rates $\tilde{\alpha}c_i$, as a function of step size and starting point of the numerical integration.

Δz	z_{start}	c_r	c_i	$\tilde{\alpha}c_i$
0.10	−10.0	−0.22690	0.00672	0.00206
0.13	−10.0	−0.22690	0.00673	0.00206
0.20	−10.0	−0.22691	0.00675	0.00207
0.20	−8.0	−0.22644	0.00650	0.00199
0.20	−10.0	−0.22691	0.00675	0.00207
0.20	−12.0	−0.22702	0.00682	0.00209

Several runs were made in order to determine an optimum mesh size and starting point for the integration scheme. The results of these runs are shown in Table 1. Studies such as the ones made here require the calculation of a great many eigenvalues. In the interests of efficiency and economy, it was desirable to use as coarse an integration mesh and as small an integration range as was compatible with the desired accuracy of the eigenvalues. A domain of integration of $-10 \leqslant z \leqslant 0$ and a mesh size of $\Delta z = 0.2$ were therefore chosen. This appears to yield accuracy in the phase speed and the growth rate to three and four decimal places, respectively. Decreasing the termination criterion by an order of magnitude did not appreciably affect the results.

Finally, a limitation of the shooting method is that it yields only one eigenvalue at a time. For any given set of parameters, there may be an entire set of discrete eigenvalues (Mack, 1976, has presented evidence that such discrete eigenvalues consist of a finite set in the case of the Orr–Sommerfeld equation for a Blasius layer). Indeed, it has been demonstrated that more than one unstable eigenvalue may exist for a given set of parameters in the free surface Ekman flow. The complete exploration of all such possible modes, stable and unstable, lies outside the scope of the present work, however.

REFERENCES

Brown, R. A., 1970: A secondary flow model for the planetary boundary layer. *J. Atmos. Sci.*, **27**, 742–757.

——, 1972: On the inflection point instability of a stratified Ekman boundary layer. *J. Atmos. Sci.*, **29**, 850–859.

Defant, A., 1961: *Physical Oceanography*, Vol. 1. Pergamon Press, 729 pp.

Etling, D., 1971: The stability of an Ekman boundary layer flow as influenced by the thermal stratification. *Beitr. Phys. Atmos.*, **44**, 168–186.

Faller, A. J., 1963: An experimental study of the laminar Ekman boundary layer. *J. Fluid Mech.*, **15**, 560–576.

——, and R. E. Kaylor, 1966: A numerical study of the instability of the laminar Ekman boundary layer. *J. Atmos. Sci.*, **23**, 466–480.

——, and ——, 1967: Instability of the Ekman spiral with applications to the planetary boundary layers. *Phys. Fluids Suppl.*, **10**, 212–219.

Hornbeck, R. W., 1975: *Numerical Methods*. Quantum Publ., 310 pp.

Iooss, G., H. B. Nielsen and H. True, 1978: Bifurcation of the stationary Ekman flow into a stable periodic flow. *Arch. Ration. Mech. Anal.*, **68**, 227–256.

Kaylor, R., and A. J. Faller, 1972: Instability of the stratified Ekman boundary layer and generation of internal waves. *J. Atmos. Sci.*, **29**, 497–509.

Lilly, D. K., 1966: On the instability of Ekman boundary flow. *J. Atmos. Sci.*, **23**, 481–494.

Mack, L., 1976: A numerical study of the temporal eigenvalue spectrum of the Blasius boundary layer. *J. Fluid Mech.*, **73**, 497–520.

Nomitsu, T., 1933: A theory of the rising stage of drift current in the ocean (Part 2). *Mem. College Sci., Univ. Kyoto*, **16**, 275–287.

Spooner, G. F., and W. O. Criminale, 1982: The evolution of disturbances in an Ekman boundary layer. *J. Fluid Mech.*, **115**, 327–346.

Tatro, P. R., and E. L. Mollo-Christensen, 1967: Experiments on Ekman layer instability. *J. Fluid Mech.*, **28**, 531–543.

Yih, C. S., 1969: *Fluid Mechanics*. McGraw-Hill, 622 pp.